



# Post-glacial climate forcing of surface processes in the Ganges–Brahmaputra river basin and implications for carbon sequestration

Christopher Hein, Valier Galy, Albert Galy, Christian France-Lanord,  
Hermann Kudrass, Tilmann Schwenk

## ► To cite this version:

Christopher Hein, Valier Galy, Albert Galy, Christian France-Lanord, Hermann Kudrass, et al.. Post-glacial climate forcing of surface processes in the Ganges–Brahmaputra river basin and implications for carbon sequestration. *Earth and Planetary Science Letters*, 2017, 478, pp.89-101. 10.1016/j.epsl.2017.08.013 . hal-02155995

**HAL Id: hal-02155995**

**<https://hal.science/hal-02155995>**

Submitted on 14 Jun 2019

**HAL** is a multi-disciplinary open access archive for the deposit and dissemination of scientific research documents, whether they are published or not. The documents may come from teaching and research institutions in France or abroad, or from public or private research centers.

L'archive ouverte pluridisciplinaire **HAL**, est destinée au dépôt et à la diffusion de documents scientifiques de niveau recherche, publiés ou non, émanant des établissements d'enseignement et de recherche français ou étrangers, des laboratoires publics ou privés.

# 1 Post-Glacial Climate Forcing of Surface Processes in the Ganges- 2 Brahmaputra River Basin and Implications for Carbon Sequestration

3  
4 Christopher J. Hein (hein@vims.edu)<sup>1,2,\*</sup>, Valier Galy (vgaly@whoi.edu)<sup>2</sup>, Albert Galy  
5 (agaly@crpg.cnrs-nancy.fr)<sup>3</sup>, Christian France-Lanord (cfl@crpg.cnrs-nancy.fr)<sup>3</sup>, Hermann  
6 Kudrass (kudrass@gmx.de)<sup>4</sup>, Tilmann Schwenk (tschwenk@uni-bremen.de)<sup>5</sup>

7  
8  
9 <sup>1</sup>*Department of Physical Sciences, Virginia Institute of Marine Science, College of William and*  
10 *Mary, Gloucester Point, VA USA*

11 <sup>2</sup>*Department of Marine Chemistry and Geochemistry, Woods Hole Oceanographic Institution,*  
12 *Woods Hole, MA USA*

13 <sup>3</sup>*Centre de recherches Pétrographiques et Géochimiques - CRPG CNRS-Université de Lorraine,*  
14 *15 rue Notre Dame des Pauvres, 54500 Vandœuvre les Nancy, France*

15 <sup>4</sup>*MARUM - Zentrum für Marine Umweltwissenschaften Universität Bremen Leobener Straße*  
16 *28359 Bremen, Germany*

17 <sup>5</sup>*Faculty of Geosciences, University of Bremen, Klagenfurter Str. 2-4, 28359 Bremen, Germany*  
18

19 \* - corresponding author  
20

## 21 Abstract

22 Climate has been proposed to control both the rate of terrestrial silicate weathering and  
23 the export rate of associated sediments and terrestrial organic carbon to river-dominated margins  
24 – and thus the rate of sequestration of atmospheric CO<sub>2</sub> in the coastal ocean – over glacial-  
25 interglacial timescales. Focused on the Ganges-Brahmaputra rivers, this study presents records of  
26 post-glacial changes in basin-scale Indian summer monsoon intensity and vegetation

composition based on stable hydrogen ( $\delta D$ ) and carbon ( $\delta^{13}C$ ) isotopic compositions of terrestrial plant wax compounds preserved in the channel-levee system of the Bengal Fan. It then explores the role of these changes in controlling the provenance and degree of chemical weathering of sediments exported by these rivers, and the potential climate feedbacks through organic-carbon burial in the Bengal Fan. An observed 40‰ shift in  $\delta D$  and a 3–4‰ shift in both bulk organic-carbon and plant-wax  $\delta^{13}C$  values between the late glacial and mid-Holocene, followed by a return to more intermediate values during the late Holocene, correlates well with regional post-glacial paleoclimate records. Sediment provenance proxies (Sr, Nd isotopic compositions) reveal that these changes likely coincided with a subtle focusing of erosion on the southern flank of the Himalayan range during periods of greater monsoon strength and enhanced sediment discharge. However, grain-size-normalized organic-carbon concentrations in the Bengal Fan remained constant through time, despite order-of-magnitude level changes in catchment-scale monsoon precipitation and enhanced chemical weathering (recorded as a gradual increase in  $K/Si^*$  and detrital carbonate content, and decrease in  $H_2O^+/Si^*$ , proxies) throughout the study period. These findings demonstrate a partial decoupling of climate change and silicate weathering during the Holocene and that marine organic-carbon sequestration rates primarily reflect rates of physical erosion and sediment export as modulated by climatic changes. Together, these results reveal the magnitude of climate changes within the Ganges-Brahmaputra basin following deglaciation and a closer coupling of monsoon strength with OC burial than with silicate weathering on millennial timescales.

**Keywords:** Indian Monsoon; Bengal Fan; Paleoclimate; Sediment Provenance; Biomarkers; Stable Isotopes

50    **Abbreviations:**

51    B-A: Bølling-Allerød interstadial period (14.7–12.7 ka)

52    BoB: Bay of Bengal

53    FA: fatty acid

54    G-B: Ganges and Brahmaputra

55    H1: Heinrich Event H1 (18–15 ka)

56    HCO: Holocene Climatic Optimum (10–6.5 ka)

57    HHC: High Himalaya Crystalline

58    ISM: Indian Summer Monsoon

59    LG: Late Glacial (24–18 ka)

60    LH: Lesser Himalaya

61    NH: Northern Hemisphere

62    OC: organic carbon

63    SoNG: Swatch of No Ground

64    THB: Trans-Himalayan Batholith

65    TSS: Tethyan Sedimentary Series

66    YD: Younger Dryas (12.9–11.7 ka)

67

68    **1. Introduction**

69           Silicate weathering, carbonate precipitation, and organic carbon (OC) burial in marine  
70    sediments, are the main mechanisms for sequestering atmospheric CO<sub>2</sub> over a range of  
71    timescales. The efficiency of these processes has long been mechanistically linked to climate, in  
72    particular temperature and rainfall, such that increased atmospheric CO<sub>2</sub> sequestration under

warm and wet conditions would act as a negative feedback, thereby contributing to global climate regulation. Rivers export silicate weathering products and terrestrial OC to the ocean, while river-dominated margins account for the majority of the global burial flux of OC, illustrating their disproportionate role in the global carbon cycle (Hedges and Oades, 1997). Over glacial-interglacial timescales, climate has been proposed to control the rate of export of terrestrial sediment and OC to these depocenters (Ludwig et al., 1998; Galy et al., 2015), as well as rates of chemical weathering, which exert a primary control on carbon sequestration (*e.g.*, West et al., 2005). Heretofore, few studies of large (continental-scale) systems have directly quantified in an integrated manner how past climate change has impacted the basin-scale weathering degree of silicate minerals exported to the coastal ocean, or the competency of those systems to export and bury OC, let alone both.

The Ganges and Brahmaputra (G-B) rivers, which drain the vast majority of the Himalayan range and Southern Tibet (Fig. 1a), convey the world's largest fluvial sediment load to the Bay of Bengal (BoB), resulting in the deposition of the world's largest delta (Kuehl et al., 2005) and the world's largest reservoir of terrigenous sediments ( $\sim 2.9 \times 10^{16}$  tons; Curray et al., 2003). Despite the generally low OC concentration in G-B sediments (typically  $< 1\%$ ), the G-B rivers are currently the largest single supplier of biospheric OC to the world's oceans (Galy et al., 2015). Coupled with excellent OC preservation in Bengal Fan sediments (Galy et al., 2007) and modest silicate weathering rates in the G-B basin (Galy and France-Lanord, 1999), this makes OC burial the leading carbon sequestration mechanism in the G-B system at short ( $\sim 1000$  years) through long ( $\sim 10$  million years) timescales (France-Lanord and Derry, 1997; Galy et al., 2007). Changes in Himalayan erosion driven by climate variability over the last 20 kyr are thus expected to have played a role in the global carbon cycle — specifically the magnitude of carbon

sequestration — following the last glacial maximum (21–19 ka). Here, we use a sediment record from the Bengal Fan following the last glacial maximum to 1) reconstruct hydroclimate variability (*i.e.*, monsoon intensity) and attendant paleovegetation changes in the G-B basin and, 2) evaluate how these variations in monsoon strength have affected weathering processes as well as sediment and carbon export (and burial) within the G-B basin / Bengal Fan system.

## **2. Regional Setting**

### ***2.1. The Indian Summer Monsoon as a driver of sediment and carbon export to the Bay of Bengal***

Water and sediment discharge from the G-B rivers are largely controlled by intense precipitation associated with the Indian Summer Monsoon (ISM), a coupled ocean-atmosphere-land climate system driven by cross-equatorial pressure gradients and amplified by land-sea thermal gradients and resulting low-level advection of warm, moisture-laden air from the Indian Ocean (Wu et al., 2012) and insulation of these air masses from the extratropics by the Himalayas (Boos and Kuang, 2010). This generates intense precipitation over western India, the BoB and the southern flank of the Himalayas during the height of the boreal summer. The ISM contributes precipitation that is relatively depleted in deuterium (commonly by >50 ‰) as compared with non-monsoon precipitation (IAEA/WHO, 2016), and accounts for a combined G-B water discharge of *ca.*  $1.7 \times 10^5 \text{ m}^3/\text{s}$ , from a boreal winter base level of  $\sim 0.2 \times 10^5 \text{ m}^3/\text{s}$  (Sinha et al., 2008)

### ***2.2. Sediment and carbon burial in the Bay of Bengal***

The primary depocenter of the G-B rivers is the Bengal Fan, the largest submarine fan in the world: it is 832–1430 km wide, extends offshore for *ca.* 3000 km, and its post-Paleocene deposits are up to ~16.5 km thick (Curray et al., 2003). Sediment and OC discharged from G-B rivers are transported by freshwater fluxes through the intertidal delta and further dispersed by tidal currents and storm-induced waves (Kuehl et al., 1997). However, for at least the last 125,000 years, the primary conduit for the transfer of large volumes of sediment to the distal fan has been the Swatch of No Ground (SoNG), a 160-km-long deep submarine canyon that penetrates well onto the continental shelf and intercepts westward shelf sediment transport (Fig. 2a) (Curray et al., 2003; Kuehl et al., 1997).

The upper SoNG serves as a temporary (decades to centuries) storage site for sediment in the Bengal Fan. Triggered by earthquakes, mass wasting and resulting turbidity currents within the SoNG convey large volumes of sediment to the middle and lower Bengal Fan through lateral sheet flow (sand-dominated) and channel overflow (turbidites) via a non-bifurcating, 2500-km long, 13-km-wide, 50-m-thick channel-levee system dominated by 5–35-cm thick sand and mud turbidites (Fig. 2; Curray et al., 2003; Schwenk et al., 2003; Weber et al., 1997).

### **3. Materials and Methods**

#### ***3.1. Sediment core sampling***

Three gravity piston cores were retrieved in 2540–2610 m water depth along the middle fan channel-levee system (Fig. 2) during the February 1994 (Expedition SO93) cruise of the R/V SONNE (Weber et al., 1997), coincident with sediment echosounder data (see supplemental materials for details). Core SO93-117KL (~12 m long) was collected from the outer levee. Core SO93-120KL (~11.5 m long) was collected further from the channel; the presence of a small

onlap-fill basin suggests that turbidites in this core were not overspilled along the profile shown in Fig. 2b, but are rather from a more northward direction. In contrast, Core SO93-118KL (~8 m long) was collected from a terrace on top of filled cut-off lobes proximal to the recent channel pathway (Fig. 2b).

The sedimentary stack presented by the three cores consists of alternating turbiditic sequences and rare thin hemipelagic layers; the latter were omitted in this study. Thirty-one samples (1–10 cm thick each) were collected for analysis (Supplemental Table 2). All samples were freeze-dried and homogenized, and aliquots collected for bulk inorganic and organic analyses, with the remainder (>90%) set aside for lipid extraction.

### 3.2. Age models

Age models are based on re-calibration of six reported radiocarbon ( $\Delta^{14}\text{C}$ ) ages derived from planktonic foraminifera (*Globigerinoides sacculifer*; Weber et al., 1997) and AMS-radiocarbon dating of planktonic foraminifera (*Globigerinoides sacculifer*, *Globigerinoides ruber*) from 18 additional sedimentary units (Supplemental Table 1). Age models were calculated in the Bayesian age-depth modeling software package Clam 2.1 (Blaauw, 2010), with extrapolation to core bottoms (Fig. 3).

### 3.3. Bulk sediment inorganic and organic analyses

Major and trace element concentrations were determined at SARM (CNRS, Nancy, France) by IPC-AES and ICP-MS and Nd and Sr isotopic compositions at CRPG (Nancy, France) by TIMS and MC-ICPMS, respectively (see supplemental materials). We combine our Sr/Nd data with those from these same sediment cores previously published in Pierson-



Wickmann et al. (2001), Galy et al. (2008a), and Lupker et al. (2013) to generate a record of sediment provenance variations at sub-millennial resolution (n=41 over 17.5 kyrs). However, due to methodological bias (see supplemental text), Nd isotopic data from Galy et al. (2008a) and Lupker et al. (2013) are excluded from further analyses.

The bulk-sediment weight-percent total-organic-carbon content (TOC) and total-nitrogen content (TN), and stable isotopic composition of bulk organic carbon ( $\delta^{13}\text{C}_{\text{TOC}}$ ) and nitrogen ( $\delta^{15}\text{N}_{\text{TN}}$ ), were analyzed for all samples (see supplemental materials for details). These data supplement existing TOC, TN, and  $\delta^{13}\text{C}_{\text{TOC}}$  data from the same cores presented by Galy et al. (2008a).

#### ***3.4. Compound-specific organic analyses***

Lipids were extracted from sample aliquots. Fatty acids (FA) were isolated and methylated using methanol (MeOH) of known D/H ( $\delta\text{D}$ ) and  $\delta^{13}\text{C}$  composition. The resulting fatty acid methyl esters (FAMES) were further purified and quantified, and the  $\delta^{13}\text{C}$  and  $\delta\text{D}$  compositions of individual homologs were measured and mass-balance corrected for the contribution of one additional carbon, and three additional hydrogen atoms per homolog during methylation. Fatty acid  $\delta\text{D}$  values ( $\delta\text{D}_{\text{FA}}$ ) were further corrected for variations in seawater isotope composition related to global ice volume variations during the deglaciation (Clark et al., 2009). The resulting ice-volume-corrected FA  $\delta\text{D}$  values ( $\delta\text{D}_{\text{FA-IV}}$ ) were then corrected for variable H isotope fractionation by each C3 and C4 vegetation endmembers to estimate precipitation  $\delta\text{D}$  values ( $\delta\text{D}_{\text{P}}$ ) (see supplemental materials for details). This approach carries significant uncertainties (on the order of  $\pm 15 \text{‰}$ ) due to the lack of adequate characterization in the G-B basin of: 1) H isotopic fractionation by the vegetation; and 2) the carbon stable-isotopic

composition of the C3 and C4 plants endmembers. Nonetheless, the core-top calculated  $\delta D_p$  value is consistent with modern isotope composition of rainfall in the floodplain/delta (IAEA/WHO, 2016) – the dominant source of plant-wax in G-B river sediments (Galy et al. 2008b) – suggesting that the fractionation factors and endmember composition we used are adequate.

#### 4. Results

Results of bulk and compound-specific  $\delta^{13}C$ ,  $\delta^{15}N$ , and  $\delta D$  values are given in Supplemental Table 2. All are reported in ‰ notation against the Vienna Pee Dee Belemnite (VPDB), air, and Vienna Standard Mean Ocean Water (VSMOW) standards, respectively. Measured major and trace inorganic elemental compositions and Sr (given as  $^{87}Sr/^{86}Sr$ ) and Nd (given as  $\epsilon Nd$ ) isotopic compositions of bulk sediment samples are given in Supplemental Table 3.

##### *4.1. Channel-levee core accretion rates: Core age models*

Linearized sediment accumulation rates range from <50 to >500 cm/kyr for the three cores. We recognize the obvious limitation of calculating linear rates in turbiditic deposits: sedimentation is episodic in nature, and therefore accumulation rates are largely controlled by mass wasting processes at the turbidite source (*i.e.*, the SoNG) as well as local hydrodynamic conditions at the depocenter.

Outer-levee cores SO93-117KL and SO93-120KL (Fig. 2b) record 16.9 and 17.5 kyrs of deposition, respectively, with long-term accumulation rates of 66–72 cm/kyr. Core SO93-120KL also shows significant peaks in sediment deposition *ca.* 10 ka (likely also evident in SO93-

117KL) and 12.8–13.6 ka (Fig. 3d); average sediment accretion at 10.2–12.8 ka was 190 cm/kyr. Following the second sediment pulse, sedimentation rates in both outer levee cores fell to among their lowest values (20–60 cm/kyr) for the remainder of the Holocene. These accumulation rates were greatly exceeded by those within the inner levee, where time-averaged Holocene accumulation rates in core SO93-118KL, capturing 9.6 ka to present, were ~120 cm/kyr.

#### 4.2. Inorganic elemental and isotopic compositions

Given the turbiditic nature of sediment deposition in the BoB channel levee, grain-size variations are expected to exhibit a first-order control on temporal organic (*e.g.*, OC concentrations) and inorganic (*e.g.*, weathering) records. Al/Si ratios provide a proxy for mineralogical composition and grain size and can be used to correct mobile-to-immobile (*e.g.*, K/Si) ratios for sorting effects to provide (*e.g.*, as K/Si\* [grain-size-corrected Si]) a temporal record of chemical weathering (Lupker et al., 2013). Al/Si ratios vary from 0.26 (“coarsest” and most quartz-rich) to 0.46 (“finest” and most phyllosilicate-rich), with most ratios >0.35 (n=64; total n=74), reflecting an intentional sampling bias towards the (fine) top of turbidites. K/Si\* ratios — combined with published data (Lupker et al., 2013) replotted with updated core age models — show a progressive decrease through time, from ~0.056 at the LG to ~0.051 at present (2 $\sigma$  standard error on K/Si\* is  $\pm$  0.0010; Fig. 4a). Likewise, Ca/Si ratios closely correspond to detrital carbonate content (supplemental fig. 5) and are interpreted as a basin-scale weathering proxy by Lupker et al. (2013); these too show a decrease across the deglaciation, from 0.073 at the LG to 0.027 in the late Holocene (Fig. 4b). A notable Ca/Si outlier at 3.7 ka (Ca/Si=0.10; omitted from Fig. 4b) is biased by marine carbonate (8.4% marine carbonate content; average for all samples is 1.2%; sample also has high Sr and Ba concentrations, low C/N ratio, highest  $\delta^{15}\text{N}$

value) and as such does not reflect continental chemical weathering. Together, K/Si\* and Ca/Si records reveal an increase in weathering of sediments exported by the G-B rivers across deglaciation; however, this may be partially influenced by changes in sediment provenance. We also note a conspicuous lack of variation in sediment weathering proxies (including  $\text{H}_2\text{O}^+/\text{Si}^*$ ; Supplemental Table 3) in the last 4000 years.

Our data demonstrate coherent temporal shifts in both  $^{87}\text{Sr}/^{86}\text{Sr}$  and  $\epsilon\text{Nd}$  compositions. Specifically,  $^{87}\text{Sr}/^{86}\text{Sr}$  ratios increase from 0.73–0.74 during the late glacial to 0.75–0.76 by the early Holocene, followed by a gradual return to intermediate values towards present (Fig. 4c). Temporal trends in Nd isotope composition generally inversely follow trends in  $^{87}\text{Sr}/^{86}\text{Sr}$  values ( $^{87}\text{Sr}/^{86}\text{Sr}$  ratios and  $\epsilon\text{Nd}$  values are generally negatively correlated) and demonstrate a general shift towards lower  $\epsilon\text{Nd}$  values through time (Fig. 4d), with noticeably higher-than-average  $\epsilon\text{Nd}$  values immediately following Heinrich Event 1 (H1) (n=3). The chemical composition (chiefly low K/Si\* and high  $\epsilon\text{Nd}$  values) of these three H1 samples is unusual compared to the rest of the dataset, suggesting they have a significant hemipelagic component more influenced by sedimentary supply from the Burmese Range in the BoB (e.g., Colin et al., 2006; Joussain et al., 2016; Supplemental Fig. 6).

#### ***4.3. Bulk organic properties and lipid distributions***

TOC and TN values, both of which are similarly dependent on sediment surface area, range from 0.4% to 0.8% (average: 0.6%) and 0.047% to 0.10% (average: 0.07%), respectively; these are weakly correlated (Supplemental Fig. 7). Resulting TOC:TN ratios range from 8.6 to 11.7 and show a small, gradual decrease through time; an anomalous high value (TOC:TN = 15.5) corresponds with the period of highest outer-levee sedimentation at 10.2–10.3 ka (Fig. 5a).

TOC values are highly sensitive to sediment grain size and bulk mineral composition (Galy et al., 2007; 2008a) and are thus normalized to sediment Al/Si. Carbon loading (OC\*) – the deviation in TOC for a given sample from the linear trend between modern Lower Meghna River sediment TOC and Al/Si values (see Galy et al., [2007, 2008b]) – was calculated independently for new samples and for those from Galy et al. (2008a) due to methodological differences (see supplemental materials and Supplemental Figs 2, 3, 4). The resulting values are discussed as relative deviations (expressed in %) with respect to modern OC loading of the Lower Meghna River, the combined outflow of the G-B rivers (Fig. 5b).

Channel-levee OC\* values show no temporal trend. Mean OC\* over the entire time period is -1% of modern mean Lower Meghna River sediments OC loading. Excluding outliers of +103%, +74%, and +58% at 8.6, 11.7, and 15.8 ka, respectively (the latter of these – the only for which we have Nd isotopic data – coincides with a H1 hemipelagic sample), all channel-levee OC\* values are well within variability of the modern river system, and within 35% of mean Lower Meghna sediments (Fig. 5b). Together, these data imply that, over the last 18 kyr, the carbon loading of sediments deposited in the channel-levee system is, on average, statistically identical to the modern river.

#### ***4.4. Paleo-vegetation and paleo-hydrology: Bulk $\delta^{13}C$ and fatty acid $\delta^{13}C$ and $\delta D$ compositions***

Relatively small differences in isotopic composition were observed among long-chain homologs (see Supplementary Table 1). C<sub>28</sub> FA, which was consistently the most abundant homolog (average concentration: 0.64 µg/g), and weighted-average C<sub>24-32</sub> FA are the focus of discussion.

Bulk  $\delta^{13}\text{C}_{\text{org}}$  values (this study and Galy et al., 2008a, re-plotted with the updated age model) record a 3–4‰ decrease between the LG and the Holocene climatic optimum (HCO), followed by a gradual return to more intermediate values (*ca.* -20.5‰) during the last 8 kyr (Fig. 6a).  $\text{C}_{28}$  FA and weighted-average  $\text{C}_{24-32}$  FA  $\delta^{13}\text{C}$  values demonstrate similar temporal trends. Between 8 ka and present,  $\delta^{13}\text{C}$  values for both  $\text{C}_{24-32}$  and  $\text{C}_{28}$  FA increased by *ca.* 1.6‰ (Fig. 6b). Weighted-average  $\text{C}_{24-32}$  and  $\text{C}_{28}$  FA  $\delta^{13}\text{C}$  and  $\delta^{13}\text{C}_{\text{org}}$  values were anomalously depleted (-30.0‰, -29.5‰, and -21.3‰, respectively) at 13.7 ka (Bølling-Allerød). All FA homologs from this sample were similarly depleted.

Ice-volume-corrected  $\text{C}_{24-32}$   $\delta\text{D}_{\text{FA-IV}}$  and  $\text{C}_{28}$   $\delta\text{D}_{\text{FA-IV}}$  increase by ~15‰ in the 2000 years following the LG, followed by a *ca.* 40‰ decrease until the HCO, and then a return towards more intermediate values of -160 to -170‰ (similar to those representatives of the early Holocene) between the HCO and present (Fig. 7).  $\delta\text{D}_{\text{FA-IV}}$  values for both  $\text{C}_{24-32}$  FA and  $\text{C}_{28}$  FA are within error through most of the record. However, they diverge in the middle to late Holocene (between *ca.* 6500 and 2500 BP), a trend largely driven by a higher degree of depletion of  $\text{C}_{28}$  FA (~9–13‰) as compared to  $\text{C}_{24}$ ,  $\text{C}_{26}$ ,  $\text{C}_{30}$ , and  $\text{C}_{32}$  homologs. Both  $\text{C}_{24-32}$  and  $\text{C}_{28}$  FA  $\delta\text{D}$  values for a single sample at 12.7 ka (Younger Dryas) are enriched by ~20‰ with respect to samples from similar time periods (Figs. 7a,b); all individual FA homologs for this time period are similarly enriched.

Precipitation D/H values ( $\delta\text{D}_\text{p}$ ) calculated from measured  $\text{C}_{24-32}$  and  $\text{C}_{28}$  FA, corrected for ice-volume and vegetation effects, increase by ~30‰ (decrease in humidity) in the 2000 years following the LG (Fig. 7c). This was followed by a gradual, ~50‰, depletion in  $\delta\text{D}$  values between 16 ka and the HCO (10–6.5 ka), consistent with increased ISM intensity. However, this trend contains substantial internal variability, with a negative excursion of 23–27‰ at 13.7 ka

and a positive excursion of 27–30 ‰ at 12.7 ka, corresponding with the Bølling-Allerød and Younger Dryas, respectively. Calculated  $\delta D_P$  values from the youngest samples, corresponding to the last 500 years, range from -30 to -40‰. These values compare favorably to measured precipitation  $\delta D$  values from the Indo-Gangetic floodplain and the G-B delta in Bangladesh (see supplemental materials). With single  $\delta^{13}C$  (13.6 ka; Bølling-Allerød) and  $\delta D$  (12.7 ka; Younger Dryas) outliers removed, there is a strong positive correlation between  $\delta D_P$  and  $\delta^{13}C$  values of both  $C_{24-32}$  ( $R^2=0.72$ ) and  $C_{28}$  ( $R^2=0.67$ ) FA (Fig. 8).

## 5. Discussion

### *5.1. Records of monsoon intensity and vegetation change within the G-B Basin since the Late Glacial*

Floodplain sediment and organic matter – and associated provenance and paleoclimate and paleovegetation signatures – exported from the G-B river basin are transferred to the BoB depositional system on sub-millennial timescales (Galy and Eglinton, 2011; Galy et al., 2011; Lupker et al., 2012, 2013). However,  $\delta^{13}C$  measurements of  $C_{24-32}$  FA and *n*-alkanes extracted from G-B river sediments reveal that modern OC is subject to extensive turnover and replacement during transit through the floodplain. This is manifested as a downstream increase in  $\delta^{13}C$  values, indicating partial degradation and replacement of the C3 vegetation signal emanating from Himalayan rivers by OC from mixed C3/C4 vegetation in the floodplain (Galy et al., 2011). Thus, environmental signatures encoded in the stable isotopic composition of plant biomarkers within the BoB channel levee system, at least at present, primarily reflect the floodplain environment.

Nonetheless, there remains a close synchronicity between records derived from mid-fan BoB archives and regional terrestrial climate reconstructions (*e.g.*, Galy et al., 2008a; Lupker et al., 2013). Likewise, our terrestrial leaf-wax paleo-precipitation (Fig. 9f) and paleo-vegetation (Fig. 9l,m) proxy records display many of the same temporal trends observed in independent proxy records of the ISM, such as those from terrestrial speleothems (Fig. 9a; Cheng et al., 2016), marine foraminifera (Fig. 9c; Weber et al., 1997; Galy et al., 2008a), and reconstructions of salinity in the northern BoB (Fig. 9d; Kudrass et al., 2001). Specifically, our leaf-wax  $\delta D$  and  $\delta^{13}C$  records document millennial-scale climate events (*e.g.*, H1, Bølling-Allerød, and Younger Dryas) as well as longer-term, orbitally-driven climate trends; these changes, and underlying mechanisms, are discussed in detail in the following sections.

#### *5.1.1. Post-glacial changes in monsoon strength in the Ganges-Brahmaputra Basin*

Changes in Northern Hemisphere (NH) summer insolation control ISM strength on orbital and sub-orbital timescales (*e.g.*, Cheng et al., 2016; Clement et al., 2001). Over shorter periods, variations in ISM strength have also been explained by changes in tropical sea surface temperatures, changes in Eurasian snow cover, and linkages with the El Niño–Southern Oscillation (*e.g.*, Vernekar et al., 1995). During the LG, reduced differential heating between the Indian Ocean and the Asian continent weakened summer circulation and produced cooler, drier conditions over Asia and across the Himalayas (Clement et al., 2001). Strengthening NH insolation during deglaciation and until the Holocene Climatic Optimum (9–5 ka) corresponded with a general increase in monsoonal activity and an increase in mean effective moisture over central Asia and in the G-B basin (Fig. 9b; Herzschuh, 2006). These variations were manifested as a general decrease in northern BoB salinity (Fig. 9c,d; Kudrass et al., 2001). These trends



have reversed as ISM strength has weakened since the mid-Holocene in response to primarily precession-driven declining NH summer insolation (Rao et al., 2016).

Over multi-annual timescales, terrestrial leaf-wax  $\delta D$  reconstructions have been demonstrated to respond to changes in precipitation amount (rather than moisture source) in the G-B basin (Contreras-Rosales et al., 2014; Rao et al., 2016). These trends are confirmed by leaf-wax proxy records presented here (Fig. 9f) and by those recently published from a sediment core on the northern BoB slope (SO188-342KL, see location, Fig. 2a) (Contreras-Rosales et al., 2014; Fig. 9e). Close temporal correlation of BoB leaf-wax records with independent proximal terrestrial and marine climate reconstructions (although there remains a disconnect with records of Arabian Sea wind variability; see, *e.g.*, Clemens et al. [2010]) indicates high sensitivity of the G-B basin and these leaf-wax proxies to changes in ISM strength during the period following the LG, and confirm earlier observations of broad regional coherence in ISM variability (Fig. 9). For example,  $\delta D_{FA-IV}$  (this study) and  $\delta D_{alk-IV}$  (Contreras-Rosales et al., 2014) reconstructions during the LG through H1 show a gradual enrichment (weakening ISM) corresponding with early stages of enhancement of NH summer insolation (Fig. 9e,f). This is a recognized feature of ISM response to the collapse of NH ice sheets: the release of cold ice and meltwater into the North Atlantic propagates through the ocean and atmosphere, reducing regional relative humidity and temporally weakening the ISM (Cheng et al., 2016).

Quantitatively, our calculated  $\delta D_P$  values from the post-LG period, and in particular H1 event ( $-7\text{‰}$ ), are suggestive of very weak summer monsoon. The modern, multidecadal  $\delta D_P$  time-series from New Delhi (IAEA/WMO, 2016) shows that such enriched  $\delta D_P$  values are currently mainly restricted to outside the summer monsoon season (*i.e.*, during the “dry” period). These New Delhi data do not show a clear dependence of  $\delta D_P$  to the annual or monthly

precipitation amount (*i.e.*, an amount effect as per Dansgaard's definition). However, a mixing of water masses characterized by drastically different isotope composition ( $\delta D_P$ , but also deuterium excess) is evident, with the summer monsoon period overall characterized by highly depleted isotope compositions (and high precipitation amount). If these observations can be transposed to past hydroclimate conditions, our calculated  $\delta D_P$  value for the H1 event requires a reduction in the amount of summer monsoon rainfall by an order of magnitude as compared to the modern period (>80% of annual precipitation), resulting in muted seasonality, and a ~3x reduction in annual precipitation amount (assuming inter-monsoon precipitation levels remained at modern levels). Such diminished precipitation is consistent with the lack of significant freshwater dilution suggested by estimates of BoB seawater salinity at the LG/H1 (Kudrass et al., 2001; Marzin et al., 2013; Fig. 9d), and is in line with the rare modern occurrence of very weak monsoons (total annual precipitation <500 mm in five of 39 years) in New Delhi, which result in much lower-than-normal seasonality and annual rainfall, and enriched annually averaged  $\delta D_P$  values (IAEA/WMO, 2016).

Our results continue to match regional ISM reconstructions well throughout the early through middle Holocene (see, *e.g.*, Rao et al., 2016 and references therein), demonstrating a period of higher humidity (more depleted  $\delta D_P$  values) during the early to early-middle Holocene, and gradually returning to more intermediate values during the last 6000 years.

In contrast, neither our, nor earlier (Contreras-Rosales et al., 2014), leaf-wax  $\delta D$  records capture the anomalous (with respect to decreasing NH summer insolation), subtle increase in monsoon strength during the past 2000 years observed in Chinese cave  $\delta^{18}O$  records (Fig. 9a; Cheng et al., 2016; Rao et al., 2016); this same shift was also not observed in atmospheric  $O_2$   $\delta^{18}O$  records (Severinghaus et al., 2009). This may indicate that the recent increase in monsoon

strength recorded in Chinese cave records is a feature of the greater amount-effect sensitivity of these sites to more subtle changes in monsoon strength due to their higher elevations and more distal locations with respect to moisture source (Botsyun et al., 2016).

#### *5.1.2. Post-glacial changes in vegetation dominance in the Ganges-Brahmaputra Basin*

Comparison of modern river sediments with those buried in the Bengal Fan channel-levee system revealed that grain-size-normalized OC concentrations remain constant from the fluvial to the marine environment and that, during deposition and burial in the modern fan, the input of marine organic matter is muted by the very large influx of terrestrial matter (Galy et al., 2007, 2008b). New bulk and compound-specific  $\delta^{13}\text{C}$  records demonstrate a remarkable positive correlation ( $R^2=0.84$ ) (Fig. 8a). Moreover, there is a lack of a systematic variation in leaf-wax contributions to the OC pool since the LG (Fig. 5c). Together, these observations confirm that the strong predominance of terrestrially-derived organic matter in BoB channel-levee sediments has persisted for at least the last 18 kyr.

Paleo-vegetation data (this study and Galy et al., 2008a; Fig. 9l) demonstrate a 3–4 ‰ shift in  $\delta^{13}\text{C}_{\text{org}}$  between H1 and the HCO, recognized as a transition of terrestrial vegetation from dominantly C4, savanna-like, to dominantly C3, forest-like, in response to increased atmospheric  $\text{CO}_2$  concentrations and decreased water stress (Galy et al., 2008a). This was followed by a gradual return to more intermediate values (*ca.* -20.5‰) during the last 8 kyr. These same trends are also captured in compound-specific  $\delta^{13}\text{C}_{\text{FA}}$  records (Fig. 9m). The relative enrichment (C4-like signal) of both  $\delta^{13}\text{C}_{\text{org}}$  and  $\delta^{13}\text{C}_{\text{FA}}$  throughout the period of study (as compared to a pure C3 Himalayan signature [modern  $\text{C}_{24-32}$  FA  $\delta^{13}\text{C}$  at base of Himalayas: min = -32.5‰; max = -30.8‰]; Galy et al., 2011) suggest that the role of OC turnover and replacement by floodplain

vegetation is a long-standing feature of this system. This observation may also explain the outlier sample corresponding with the Bølling-Allerød at 13.6 ka, which has a strongly depleted  $\delta^{13}\text{C}_{\text{FA}}$  and somewhat depleted  $\delta\text{D}_{\text{P}}$  signal, possibly suggesting an excess Himalayan OC input at this time; this is further supported by sediment provenance data (see section 5.2). We posit that this sample may capture a short-lived period of rapid and direct (*i.e.*, without time for floodplain organic matter turnover) discharge of sediment and OC from the upper Brahmaputra basin associated with megaflood discharge on the Tsangpo River, similar to other well-documented episodes during this time (*e.g.*, Huang et al., 2014).

There is close correspondence between C3/C4 vegetation composition as reflected in  $\delta^{13}\text{C}_{\text{FA}}$  values and precipitation isotope composition as reflected in  $\delta\text{D}_{\text{FA-IV}}$  records (Fig. 8b). This correlation reflects the combined effect of precipitation regime changes driving a corresponding change in vegetation type, and the differential fractionation of stable hydrogen isotopes by different photosynthetic pathways of each C3 and C4 vegetation; derivation of  $\delta\text{D}_{\text{P}}$  attempts to remove some of the latter factor. Comparison of  $\delta^{13}\text{C}_{\text{FA}}$  (Fig. 9m) and  $\delta\text{D}_{\text{P}}$  (Fig. 9f) records reveals close temporal correspondence; that is, there is a relatively rapid (centennial or shorter) response of vegetation composition to hydroclimate changes.

## ***5.2. Concurrent Himalayan Climatic and Sediment Provenance Shifts since the Late Glacial***

The lithological diversity of the G-B basin is reflected in markedly different Sr and Nd isotopic signatures of source rocks in its major geological terranes (Fig. 1b). Modern G-B sediment is dominated by mixing between four primary sources: (1) Trans-Himalayan Batholith (THB), with relatively high  $\epsilon\text{Nd}$  values (*ca.* -5 to -8) and low  $^{87}\text{Sr}/^{86}\text{Sr}$  ratios (*ca.* 0.70–0.72); (2) Tethyan Sedimentary Series (TSS), with lower  $\epsilon\text{Nd}$  values (*ca.* -10 to -17) and higher  $^{87}\text{Sr}/^{86}\text{Sr}$

ratios (*ca.* 0.72–0.73); (3) Lesser Himalaya (LH), with low  $\epsilon\text{Nd}$  values (*ca.* -22 to -28) and high  $^{87}\text{Sr}/^{86}\text{Sr}$  ratios (*ca.* 0.81–0.92); and (4) High Himalaya Crystalline (HHC) ( $\epsilon\text{Nd}$ : -12 to -17;  $^{87}\text{Sr}/^{86}\text{Sr}$ : 0.73–0.77), whose intermediate  $^{87}\text{Sr}/^{86}\text{Sr}$  and  $\epsilon\text{Nd}$  compositions falls off the THB-LH and TSS-LH mixing trends (Fig. 10 inset) (Bouquillon et al., 1990; France-Lanord, et al., 1993; Galy and France-Lanord, 1999; Galy et al., 1999; Galy et al., 2010; Lupker et al., 2013; Robinson et al., 2001; Singh et al., 2008). Furthermore, Himalayan terrains have a unique Sr and Nd isotopic signature as compared to other potential sediment sources to the BoB (*e.g.*, Galy et al., 2010). Given the quasi-exclusive G-B sediment source to the BoB channel-levee system, Sr and Nd isotopic data are expected to approximate a multi-member mixing model, reflecting changes in sediment provenance and, hence, erosion distribution within the Himalayan range through time. Thus, assuming transport and delivery mechanisms of sediment from the G-B mouth to the BoB channel-levee system have remained constant with respect to the transference of Sr and Nd isotopic signatures, these proxies can be used to track relative changes in Bengal Fan sediment provenance through time (at least since deglaciation).

Several records have demonstrated that, following the LG and into the early Holocene, enhanced erosion in the High Himalayas increased sediment export — notably that derived from HHC and LH terranes — to the coast (*e.g.*, Bookhagen et al., 2005; Clift et al., 2008; Goodbred and Kuehl, 2000). However, other post-glacial provenance reconstructions from the upper BoB channel-levee system indicated that the balance between sediment derived from various Himalayan terranes has remained relatively stable and consistent with modern mixing (Galy et al., 2008a; Lupker et al., 2013; Pierson-Wickmann et al., 2001). Our data present the first record from which paleo-precipitation and provenance and weathering proxies are derived from the same sediments. While the HHC remains the dominant source of sediment (akin to the modern

G-B river system), these records — particularly  $^{87}\text{Sr}/^{86}\text{Sr}$  compositions (Figs 4c, 9j), which are less sensitive to hemipelagic contributions than  $\epsilon\text{Nd}$  values — reveal small to moderate source variations through time. Specifically, during warmer, wetter periods — as reflected by  $\delta\text{D}_\text{p}$  — Sr and Nd isotope compositions reflect roughly equivalent mixing between LH (Himalaya Front Range) and THB (Tibetan Plateau) sources and enhanced contribution of sediment from the HHC (located between the LH and THB terranes; see Fig. 1b), whereas during cooler, drier periods, there is relatively enhanced THB and/or TSS sourcing, at the expense of HHC and LH contributions (Figs. 9, 10). A single outlier at 13.6 ka (Bølling-Allerød) is likewise highly depleted in deuterium and  $^{13}\text{C}$  and has a sediment Sr and Nd isotopic composition which closely approximates THB-dominated THB/LH/HHC mixing, again suggesting that this sample may capture a large discharge event from the THB-dominated upper Brahmaputra / Tsangpo drainage basin.

Among a range of possible explanations for this subtle post-glacial correlation between climate and sediment provenance, several are most likely given observed trends. Following the LG, meltwater (loaded with OC-poor, mechanically eroded glacial flour) from more expansive glaciers across the high-elevation TSS (see location, Fig. 1b) may have contributed more to the water discharge, especially given lower overall discharge associated with a relatively weak ISM, thereby providing for relatively enhanced export of TSS-derived sediment. Such a scenario would account for the relatively low degree of chemical weathering observed in BoB channel levee sediments deposited during periods of enhanced export during the latest Pleistocene to early Holocene. Moreover, this sediment would have been relatively OC-depleted, allowing for acquisition of OC, and its attendant isotopic signatures, during its transit through the floodplain. Alternatively (or additionally), strengthening of the ISM during the late Pleistocene and early

Holocene led to focusing of rainfall on the HHC and LH. Enhanced rainfall on land recently exposed by shrinking glaciers in the high elevation HHC removed large volumes of mechanically eroded, glacially liberated sediment from this system, enhancing HHC contributions to overall G-B sediment discharge. This would have been at the relative expense of the THB and/or TSS, a process observed over shorter time periods (Bookhagen et al., 2005). This hypothesis is supported by Clift et al. (2008) who found that, although ISM strength closely controls erosion rates in both the LH and HHC, the effect was larger for the southerly LH. Thus, Sr and Nd provenance proxy shifts may indicate enhanced precipitation focusing on the Himalayan Front Range and decreased meltwater contributions, and not (only) an increase in sediment export from formerly glaciated regions of the High Himalayas.

### ***5.3. Controls on post-glacial organic carbon burial in the Bengal Fan***

Despite being organic-poor (average: < 0.5% OC; Galy et al., 2007), the enormous sediment volume from the G-B rivers leads to a terrestrial biospheric OC burial flux of  $\sim 3.9 \times 10^{11}$  mol/yr, that is *ca.* 20% of the modern global total (Galy et al., 2007, 2011). This is also sustained by high burial efficiency; that is, the modern G-B rivers retain consistent OC loads through burial in the Bengal Fan (Galy et al., 2007). Our data reveal that, despite substantial changes in paleohumidity (section 5.1.1), vegetation composition (5.1.2), and monsoon focusing (section 5.2) over the last 18,000 years, sediment OC loading in the Bengal Fan has remained roughly constant and within 35% of modern values since the LG (Fig. 5b). Temporal changes in OC burial rates at the middle Bengal Fan channel-levee system during this time are thus controlled predominantly by changes in sediment discharge and burial rates.

Carbon-export and burial rates are also independent of the degree of chemical weathering of these same sediments (see section 4.2 and Supplemental Fig. 9): assuming  $K/Si^*$ ,  $Ca/Si$ , detrital carbonate content, and  $H_2O^+/Si^*$  ratios are indeed valid proxies for the degree of chemical weathering at the catchment scale, weathering intensity increases gradually and unidirectionally through time. By contrast,  $OC^*$  values remain within a narrow range and show no temporal trend. Thus, we conclude that, whereas OC loading is independent of climate, the export and burial of OC in the BoB primarily reflects sediment export and burial rates – and thus terrestrial *physical* erosion rates –since the LG. This outcome is in line with recent findings for the modern global fluvial carbon export (Galy et al., 2015). In the G-B basin, this erosion / carbon-sequestration coupling is modulated by climate-geomorphological interactions in response to, for example, precipitation amount, rainfall, and erosion focusing.

By contrast, the final depocenter – and thus the rate and depth of burial – of this OC is controlled by river, shelf, and slope sediment transport processes. At lower stands of sea level associated with the LG, the confluent G-B river discharged directly into the SoNG and from there directly conveyed sediment and OC to the Bengal Fan (Kuehl et al., 2005), including to the channel-levee system of the middle fan. Following the Younger Dryas, rapid sea-level rise resulted in the flooding of the shelf, severing of the direct connection between the G-B rivers and the SoNG, trapping of sediment on the flooded Bengal margin, and the onset of widespread subaerial and subaqueous delta aggradation (Goodbred and Kuehl, 2000; Weber et al., 1997). Nonetheless, the levee system continued to receive sediment and OC throughout the Holocene, as evidenced by continued accumulation at rates of 20–60 cm/kyr. In fact, unlike many of the large modern fans (*e.g.*, Mississippi, Amazon, Rhone, Indus), the continued, rapid transfer of



sediment from the G-B rivers to the head of the SoNG has allowed the Bengal Fan to continue to develop and bury large volumes of OC during the present highstand (Weber et al., 1997).

## **6. Summary and Conclusions**

This study presents the first post-glacial paleo-precipitation and paleo-vegetation records from the G-B basin. Our records generally confirm trends observed by earlier regional studies of ISM evolution: during the late glacial, reduced differential heating between the Indian Ocean and the Asian continent weakened summer circulation and produced cooler, drier conditions over the northern BoB, Indo-Gangetic plain and across the Himalaya. Increasing NH insolation during deglaciation and through the mid-Holocene corresponded with an increase in atmospheric CO<sub>2</sub> concentrations, mean effective moisture, and monsoonal activity, and a large decline of C4 plants, in the G-B basin. Our data also compare favorably with earlier records in their ability to capture shorter-term variability in precipitation and vegetation dominance associated with, *e.g.*, the H1, Bølling-Allerød, and Younger Dryas. Our data do, however, demonstrate a larger amplitude of variation than seen in earlier studies (Contreras-Rosales et al., 2014), possibly reflecting the pure G-B signal transferred to the BoB channel-levee system – as opposed to the mixed sources for the Eastern Bengal Slope (Contreras-Rosales et al., 2016; see supplemental materials for complete discussion) – and the likelihood of contributions from outside the G-B basin to the BoB slope and shelf.

In contrast to earlier studies, we find that these climate changes have resulted in notable variations in source contributions to integrated G-B basin sediment export. Specifically, a combination of availability of glacially liberated sediment and monsoon-driven rainfall focusing may have led to higher rates of export from HHC and LH terranes during the recorded period of

greatest monsoon strength during latest Pleistocene and early Holocene. In contrast, sediment delivered to the BoB during colder and drier periods (as recorded in concurrent paleoclimate and paleovegetation records) following the LG has a provenance signature suggestive of reduced export from the LH terrane in the South flank of the range. These findings – though not conclusive with regard to responsible mechanisms for observed provenance changes – together highlight the importance and utility of developing concurrent records of paleo-environmental changes and sediment provenance.

Finally, despite significant changes in climate, sediment provenance, and transport mechanisms of sediment and organic matter from the G-B river mouth to its depocenter in the middle Bengal Fan since the LG, we demonstrate that carbon loading – and thus sediment-volume and grain-size- normalized burial rates – has remained within the narrow range of the modern rivers through time. Burial rates respond almost exclusively to sediment deposition rates, which are in turn largely controlled by monsoon strength and sea level. In contrast, variations in the degree of chemical weathering of sediment exported by the G-B rivers do not follow climate variations in a straightforward manner, as previously observed over longer timescales (Wilson et al., 2015), thus demonstrating the possible late Holocene decoupling of climate forcing and silicate weathering in the Himalayas. These findings reveal the primacy of physical erosion (as opposed to chemical weathering) and sediment transport mechanisms – modulated by climate variability, monsoon focusing, and sea-level change following deglaciation – in controlling sediment / OC export from G-B system, and thus the burial and sequestration of OC within the BoB marine archive. These outcomes together demonstrate a closer coupling between post-glacial variations in monsoon strength and OC burial than between changes in monsoon strength and silicate weathering, and further highlight the potential importance of climatic controls on

physical processes within the G-B system — and more broadly other highly erosive systems —  
in the medium-term (glacial-interglacial) global carbon cycle.

## 7. Acknowledgements

We acknowledge Sarah Feakins and two anonymous reviewers for comments which  
improved this manuscript, and Xavier Philippon, Carl Johnson, and Sean Sylva of WHOI for  
assistance with laboratory and isotope analysis. This work was supported by the National  
Science Foundation [grant numbers OCE-1333826 and OCE-1333387]. This is contribution  
#xxx of the Virginia Institute of Marine Science.

## 8. References

- Blaauw, M., 2010. Methods and code for ‘classical’ age-modelling of radiocarbon sequences,  
*Quaternary Geochronology*, v. 5, p.512-518.
- Blair, N.E. and Aller, R.C., 2012. The fate of terrestrial organic carbon in the marine  
environment, *Annual Review of Marine Science*, v. 4, p. 401-423.
- Botsyun, S., Sepulchre, P., Risi, C. and Donnadieu, Y., 2016. Impacts of Tibetan Plateau uplift  
on atmospheric dynamics and associated precipitation  $\delta^{18}\text{O}$ , *Climate of the Past*, v. 12,  
p.1401-1420.
- Bookhagen, B., Thiede, R.C. and Strecker, M.R., 2005. Late Quaternary intensified monsoon  
phases control landscape evolution in the northwest Himalaya, *Geology*, v. 33, p.149-152.
- Boos W.R. and Kuang Z., 2010. Dominant control of the South Asian monsoon by orographic  
insulation versus plateau heating, *Nature*, v. 463, p. 218–223.
- Bouquillon, A., France-Lanord, C., Michard, A. and Tiercelin, J.J., 1987. Sedimentology and  
isotopic chemistry of the Bengal Fan sediments: The denudation of the Himalaya. *In*:  
Cochran, J.R., Stow, D.A.V., Auroux, C., Amano, K., Balson, P.S., Boulégue, J.J., Brass,

599 G.W., Corrigan, J., Gartner, S., Hall, S., Iaccarino, S., Ishizuka, T., Decima, F.P., Raman,  
600 C.V., Sager, W.W., Takahasi, K., Thompson, T.L., Tiercelin, J.-J., Townsend, M.R., Wetzell,  
601 A., Wijayananda, N.P., and Williams, C. (eds), *Proceedings of the Ocean Drilling Program:*  
602 *Scientific Results Volume 116*, College Station, Texas: Ocean Drilling Program, p. 43-58.

603 Cheng, H., Edwards, R.L., Sinha, A., Spötl, C., Yi, L., Chen, S., Kelly, M., Kathayat, G., Wang,  
604 X., Li, X. and Kong, X., 2016. The Asian monsoon over the past 640,000 years and ice age  
605 terminations, *Nature*, v. 534, p.640-646.

606 Clark, P.U., Dyke, A.S., Shakun, J.D., Carlson, A.E., Clark, J., Wohlfarth, B., Mitrovica, J.X.,  
607 Hostetler, S.W. and McCabe, A.M., 2009. The last glacial maximum, *Science*, v. 325, p.710-  
608 714.

609 Clemens, S.C., Prell, W.L. and Sun, Y., 2010. Orbital-scale timing and mechanisms driving Late  
610 Pleistocene Indo-Asian summer monsoons: Reinterpreting cave speleothem  $\delta^{18}\text{O}$ ,  
611 *Paleoceanography*, v. 25, PA4207.

612 Clement, A.C., Cane, M.A. and Seager, R., 2001. An Orbitally Driven Tropical Source for  
613 Abrupt Climate Change, *Journal of Climate*, v. 14, p.2369-2375.

614 Clift, P.D., Giosan, L., Blusztajn, J., Campbell, I.H., Allen, C., Pringle, M., Tabrez, A.R.,  
615 Danish, M., Rabbani, M.M., Alizai, A. and Carter, A., 2008. Holocene erosion of the Lesser  
616 Himalaya triggered by intensified summer monsoon, *Geology*, v. 36, p.79-82.

617 Colin, C., Turpin, L., Blamart, D., Frank, N., Kissel, C., and Duchamp, S., 2006. Evolution of  
618 weathering patterns in the Indo-Burman Ranges over the last 280 kyr: Effects of sediment  
619 provenance on  $^{87}\text{Sr}/^{86}\text{Sr}$  ratios tracer, *Geochemistry, Geophysics, Geosystems*, v. 7, Q03007.

620 Contreras-Rosales, L.A., Jennerjahn, T., Tharammal, T., Meyer, V., Lückge, A., Paul, A., and  
621 Schefuß, E., 2014. Evolution of the Indian Summer Monsoon and terrestrial vegetation in the  
622 Bengal region during the past 18 ka, *Quaternary Science Reviews*, v. 102, p. 133-148.

623 Contreras-Rosales, L.A., Schefuß, E., Meyer, V., Palamenghi, L., Lückge, A. and Jennerjahn,  
624 T.C., 2016. Origin and fate of sedimentary organic matter in the northern Bay of Bengal  
625 during the last 18ka, *Global and Planetary Change*, v. 146, p. 53-66.

626 Curray, J.R., Emmel, F.J., and Moore, D.G., 2003. The Bengal Fan: morphology, geometry,  
627 stratigraphy, history and processes, *Marine and Petroleum Geology*, v. 19, p. 1191-1223.

628 Fournier, L., Fauquembergue, K., Zaragosi, S., Zorzi, C., Malaizé, B., Bassinot, F., Joussain, R.,  
629 Colin, C., Moreno, E., and Leparmentier, F., 2016. The Bengal Fan: External controls on the  
630 Holocene Active Channel turbidite activity, *The Holocene*, 0959683616675938.

631 France-Lanord, C., and Derry, L.A., 1997. Organic carbon burial forcing of the carbon cycle  
632 from Himalayan erosion, *Nature*, v. 390 p. 65-67.

633 France-Lanord, C., Derry, L. and Michard, A., 1993. Evolution of the Himalaya since Miocene  
634 time: isotopic and sedimentological evidence from the Bengal Fan, *Geological Society,*  
635 *London, Special Publications*, v. 74, p.603-621.

636 Galy, A. and France-Lanord, C., 1999. Weathering processes in the Ganges–Brahmaputra basin  
637 and the riverine alkalinity budget, *Chemical Geology*, v. 159, p.31-60.

638 Galy, A., France-Lanord, C., and Derry, L.A., 1999. The strontium isotopic budget of Himalayan  
639 rivers in Nepal and Bangladesh, *Geochimica et Cosmochimica Acta*, v. 63, p. 1905-1925.

640 Galy, V., and Eglinton, T.I., 2011. Protracted storage of biospheric carbon in the Ganges-  
641 Brahmaputra basin. *Nature Geoscience*, v. 4, p. 843-847.

642 Galy, V., Eglinton, T., France-Lanord, C., and Sylva, S., 2011. The provenance of vegetation and  
643 environmental signatures encoded in vascular plant biomarkers carried by the Ganges-  
644 Brahmaputra rivers. *Earth and Planetary Science Letters*, v. 304, p. 1-12.

645 Galy, V., France-Lanord, C., Beyssac, O., Faure, P., Kudrass, H. and Palhol, F., 2007. Efficient  
646 organic carbon burial in the Bengal fan sustained by the Himalayan erosional system, *Nature*,  
647 v. 450, p.407-410.

648 Galy, V., François, L., France-Lanord, C., Faure, P., Kudrass, H., Palhol, F. and Singh, S.K.,  
649 2008a. C4 plants decline in the Himalayan basin since the Last Glacial Maximum,  
650 *Quaternary Science Reviews*, v. 27, p.1396-1409.

651 Galy, V., France-Lanord, C. and Lartiges, B., 2008b. Loading and fate of particulate organic  
652 carbon from the Himalaya to the Ganga–Brahmaputra delta, *Geochimica et Cosmochimica*  
653 *Acta*, v. 72, p.1767-1787.

654 Galy, V., France-Lanord, C., Peucker-Ehrenbrink, B., and Huyghe, P., 2010. Sr-Nd-Os evidence  
655 for a stable erosion regime in the Himalaya during the past 12 Myr, *Earth and Planetary*  
656 *Science Letters*, v. 290, p. 474-480.

657 Galy, V., Peucker-Ehrenbrink, B. and Eglinton, T., 2015. Global carbon export from the  
658 terrestrial biosphere controlled by erosion, *Nature*, v. 521, p. 204-207.

659 Goodbred, S.L., and Kuehl, S.A., 2000. Enormous Ganges-Brahmaputra sediment discharge  
660 during strengthened early Holocene monsoon, *Geology*, v. 28, p. 1083-1086.

661 Hedges, J.I., Oades, J.M., 1997. Comparative organic geochemistries of soils and marine  
662 sediments, *Organic Geochemistry*, v. 27, p. 319-361.

663 Herzsuh, U., 2006. Palaeo-moisture evolution in monsoonal Central Asia during the last  
664 50,000 years, *Quaternary Science Reviews*, v. 25, p. 163-178.

665 Huang, S.Y., Chen, Y.G., Burr, G.S., Jaiswal, M.K., Lin, Y.N., Yin, G., Liu, J., Zhao, S. and  
666 Cao, Z., 2014. Late Pleistocene sedimentary history of multiple glacially dammed lake  
667 episodes along the Yarlung-Tsangpo river, southeast Tibet. *Quaternary Research*, v. 82,  
668 p.430-440.

669 IAEA/WMO (2016). Global Network of Isotopes in Precipitation. The GNIP Database.  
670 Accessible at: <http://www.iaea.org/water>

671 Kudrass, H.R., Hofmann, A., Doose, H., Emeis, K. and Erlenkeuser, H., 2001. Modulation and  
672 amplification of climatic changes in the Northern Hemisphere by the Indian summer  
673 monsoon during the past 80 ky, *Geology*, v. 29, p.63-66.

674 Kuehl, S.A., Levy, B.M., Moore, W.S. and Allison, M.A., 1997. Subaqueous delta of the  
675 Ganges-Brahmaputra river system, *Marine Geology*, v. 144, p.81-96.

676 Kuehl, S.A., Allison, M.A., Goodbred, S.L., and Kudrass, H., 2005. The Ganges-Brahmaputra  
677 Delta. In: Giosan, L., and Bhattacharya, J.P. (eds), *River Deltas: Concepts, Models and*  
678 *Examples*. Journal of the Society for Sedimentary Geology (SEPM) Special Publication No.  
679 83, p. 413–434,

680 Ludwig, W., Amiotte-Suchet, P., Munhoven, G. and Probst, J.L., 1998. Atmospheric CO<sub>2</sub>  
681 consumption by continental erosion: Present-day controls and implications for the last glacial  
682 maximum, *Global and Planetary Change*, v. 16, p.107-120.

683 Lupker, M., Blard, P.H., Lave, J., France-Lanord, C., Leanni, L., Puchol, N., Charreau, J. and  
684 Bourlès, D., 2012. <sup>10</sup>Be-derived Himalayan denudation rates and sediment budgets in the  
685 Ganga basin, *Earth and Planetary Science Letters*, v. 333, p.146-156.

686 Lupker, M., France-Lanord, C., Galy, V., Lavé, J. and Kudrass, H., 2013. Increasing chemical  
687 weathering in the Himalayan system since the Last Glacial Maximum, *Earth and Planetary*  
688 *Science Letters*, v. 365, p.243-252.

689 Marzin, C., Kallel, N., Kageyama, M., Duplessy, J.C., and Braconnot, P., 2013. Glacial  
690 fluctuations of the Indian monsoon and their relationship with North Atlantic climate: new  
691 data and modelling experiments. *Climate of the Past*, v. 9, p. 2135-2151.

692 Pierson-Wickmann, A.-C., Reisberg, L., France-Lanord, C., and Kudrass, H., 2001. Os-Sr-Nd  
693 results from sediments in the Bay of Bengal: Implications for sediment transport and the  
694 marine Os record, *Paleoceanography*, v. 16, p. 435-444.

695 Rao, Z., Li, Y., Zhang, J., Jia, G. and Chen, F., 2016. Investigating the long-term palaeoclimatic  
696 controls on the  $\delta D$  and  $\delta^{18}O$  of precipitation during the Holocene in the Indian and East  
697 Asian monsoonal regions, *Earth-Science Reviews*, v. 159, p.292-305.

698 Robinson, D.M., Decelles, P.G., Patchett, P.J., and Garzione, C.N., 2001. The kinematic  
699 evolution of the Nepalese Himalaya interpreted from Nd isotopes, *Earth and Planetary*  
700 *Science Letters*, v. 192, p. 507– 521.

- 701 Schwenk, T., Spieß, V., Hübscher, C., and Breitzke, M., 2003. Frequent channel avulsions within  
702 the active channel–levee system of the middle Bengal Fan—an exceptional channel–levee  
703 development derived from Parasound and Hydrosweep data, *Deep Sea Research Part II:  
704 Topical Studies in Oceanography*, v. 50, p.1023-1045.
- 705 Severinghaus, J.P., Beaudette, R., Headly, M.A., Taylor, K. and Brook, E.J., 2009. Oxygen-18 of  
706 O<sub>2</sub> records the impact of abrupt climate change on the terrestrial biosphere. *Science*,  
707 324(5933), pp.1431-1434.
- 708 Singh, S., Rai, S., Krishnaswami, S., 2008. Sr and Nd isotopes in river sediments from the Ganga  
709 Basin: Sediment provenance and spatial variability in physical erosion, *Journal of  
710 Geophysical Research*, v. 113, F03006.
- 711 Vernekar, A.D., Zhou, J., Shukla, J., 1995. The effect of Eurasian snow cover on the Indian  
712 monsoon, *Journal of Climate*, v. 8, p. 248–266.
- 713 Weber, M.E., Wiedicke, M.H., Kudrass, H.R., Hübscher, C., and Erlenkeuser, H., 1997. Active  
714 growth of the Bengal Fan during sea-level rise and highstand, *Geology*, v. 25, p. 315-318.
- 715 West, A.J., Galy, A. and Bickle, M., 2005. Tectonic and climatic controls on silicate weathering,  
716 *Earth and Planetary Science Letters*, v. 235, p.211-228.
- 717 Wilson, D.J., Galy, A., Piotrowski, A.M. and Banakar, V.K., 2015. Quaternary climate  
718 modulation of Pb isotopes in the deep Indian Ocean linked to the Himalayan chemical  
719 weathering, *Earth and Planetary Science Letters*, v. 424, p.256-268.
- 720 Wu, G.X., Liu, Y., He, B., Bao, Q., Duan, A., and Jin, F.-F., 2012. Thermal controls on the  
721 Asian summer monsoon. *Scientific Reports*, v. 2, p. 404.



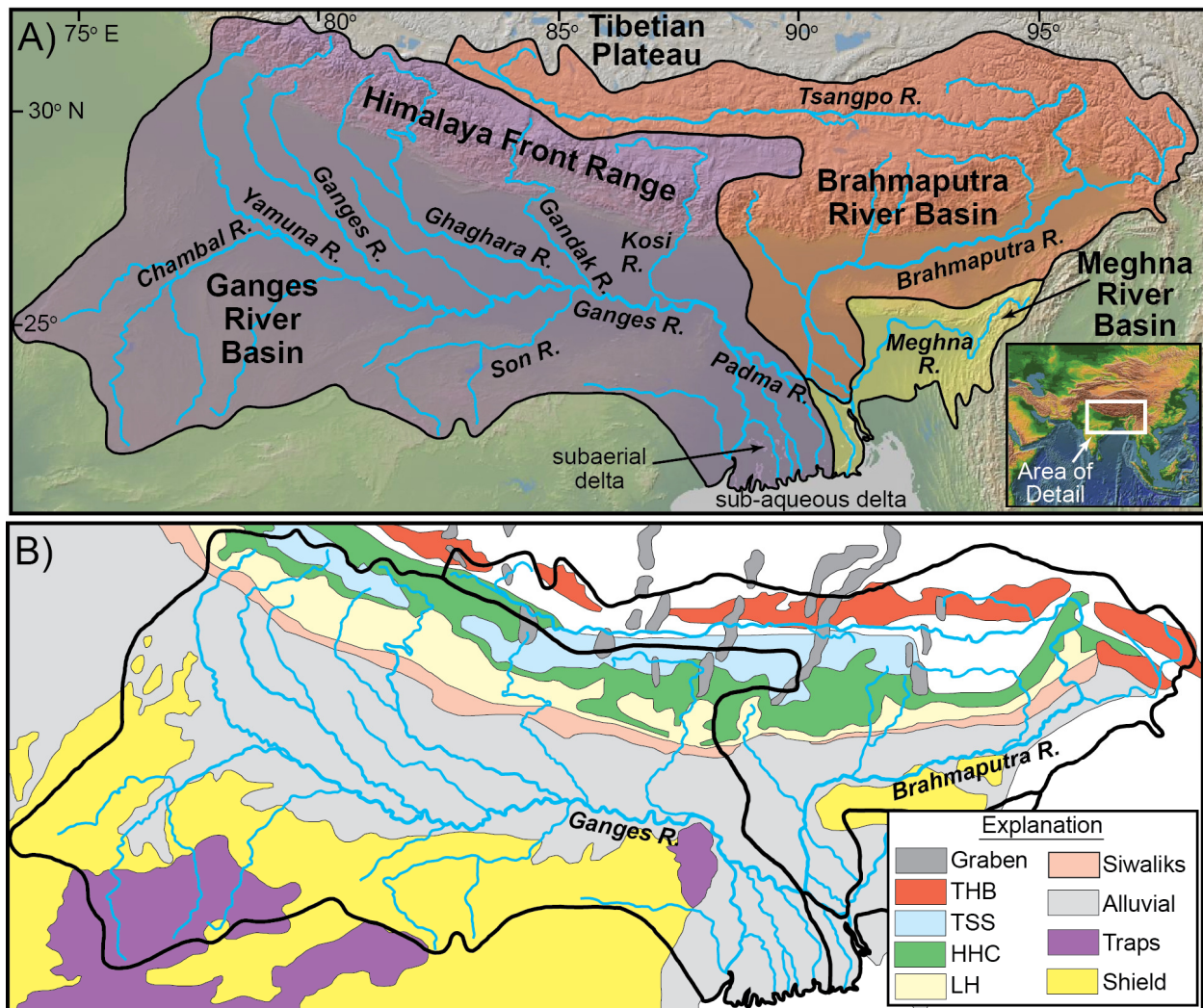


**Figure 1.** (a) Major features and tributaries of the Ganges-Brahmaputra (G-B) drainage basin. Background topographic image from GeoMapApp. (b) Geologic map of the G-B basin showing locations of the major terranes (modified from Galy et al., 2010). THB: Trans-Himalaya Batholith, TSS: Thetisian Sedimentary Series, HHC: High Himalaya Crystalline, LH: Lesser Himalaya.

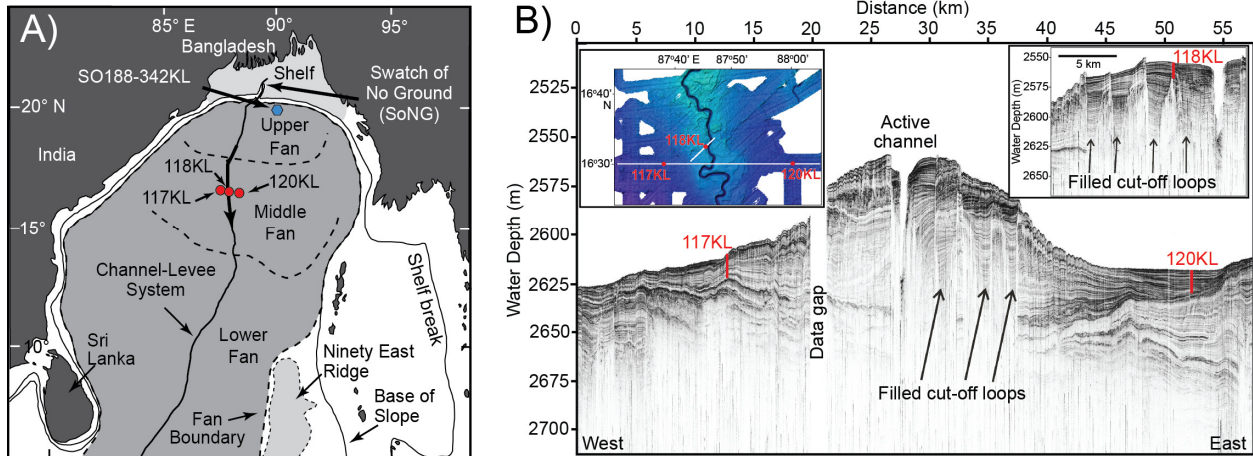


**Figure 2.** (a) Morphology of the Bengal Fan. Sediment is dominantly delivered via turbidity currents that travel along single-channel channel-levee system. Red circles: locations of 3 cores proposed for use in this study (Kudrass, 1996); blue circle: location of core SO188-342KL (Contreras-Rosales et al., 2014, 2016). (b) Parasound seismic-reflection profile crossing cores SO93- 117KL and 120KL from west to east. Upper left inset shows locations of the profile and cores with respect to the pathway of the active channel imaged by multibeam bathymetry. Upper right inlet shows Parasound data around Core SO93-118 KL, which is located 5 km to the north. These data reveal the typical architecture of a channel-levee system built by turbidity currents with a gull-wing shape and reflections diverging within the levee towards the channel. Both levees show sediment waves resulting from the overspilling turbidity currents. The system can be separated into undisturbed outer levees surrounding the inner area consisting of the active channel and filled cut-off loops, as described in detail by Schwenk et al. (2003).

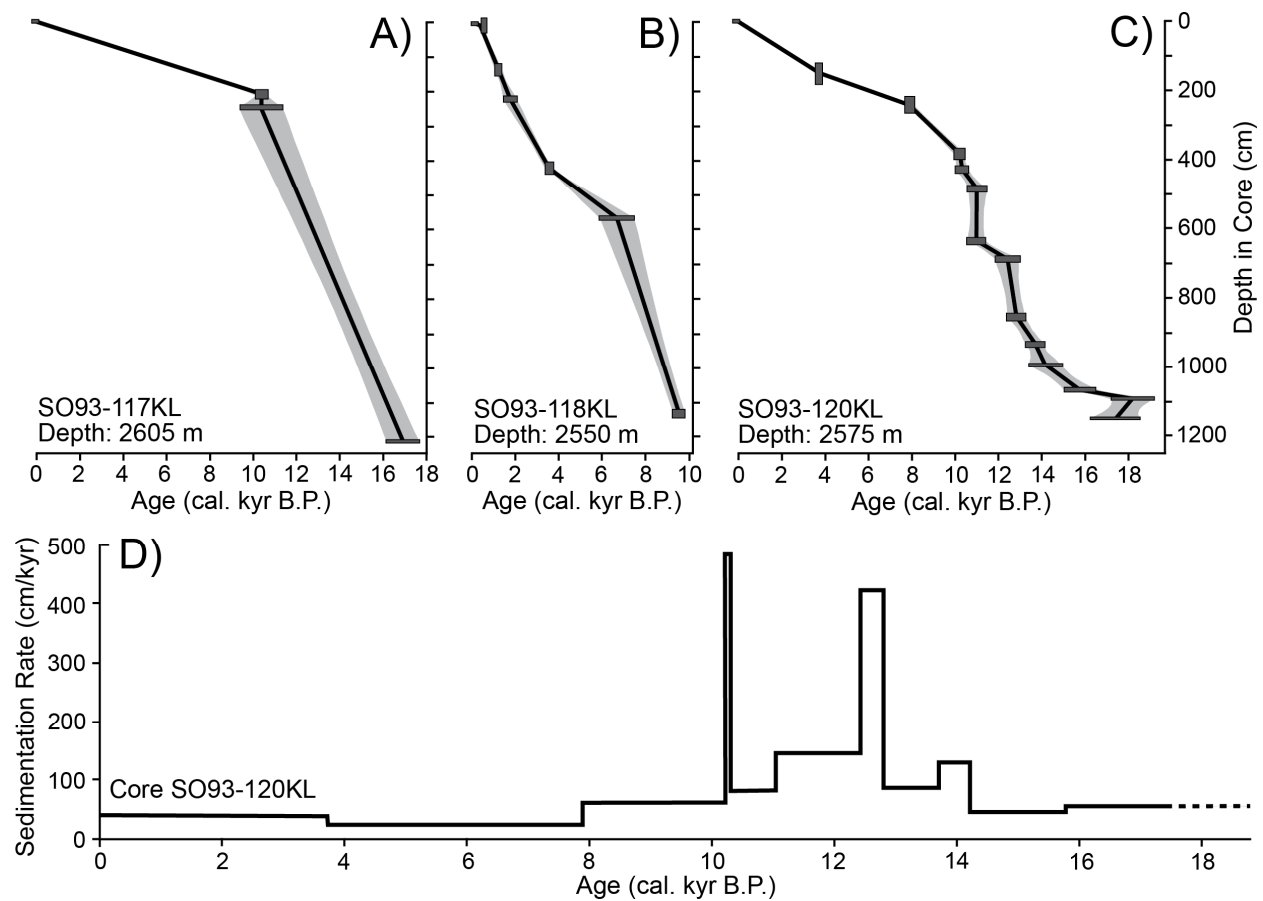


**Figure 3.** Age models for Bengal Fan channel-levee cores (a) SO93-117KL; (b) SO93-118KL; and (c) SO93-120KL, derived through linear interpolation between calibrated  $\Delta^{14}\text{C}$  ages (Table 1) and extrapolation to core tops and bottoms. Box widths represent sample depth interval within core; heights represent calibrated age error. (d) Linear sedimentation rates calculated from published and new age control points based on core SO93-120KL, the core with the highest-resolution age model.

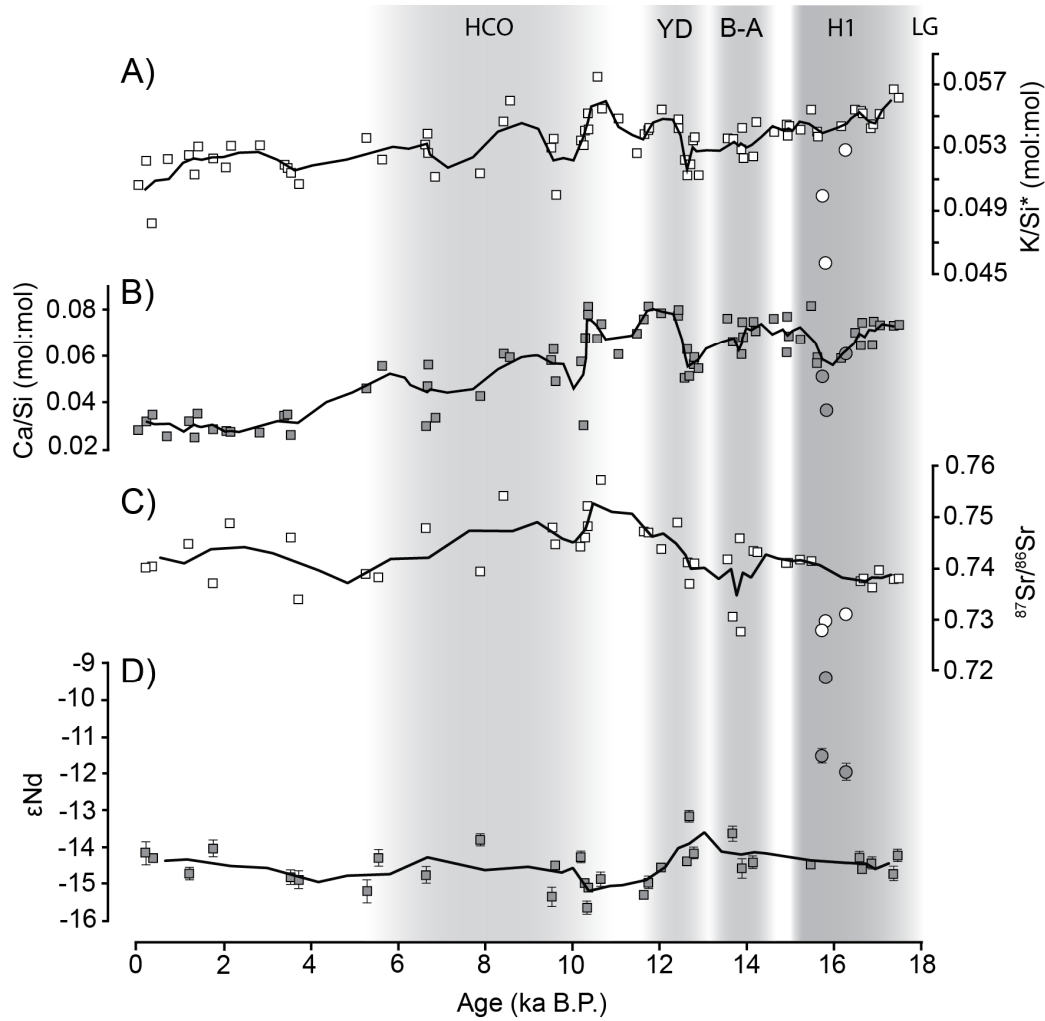


**Figure 4.** Temporal records of weathering ( $K/Si^*$  [a];  $Ca/Si$  [b]) and sediment source (strontium [c] and [d] neodymium stable isotopic compositions) from BoB channel levee cores SO93-117KL, -118KL, and -120KL. Data are from Galy et al. (2008a), Galy et al. (2014), Lupker et al. (2013), Pierson-Wickman et al. (2001), and this study.  $\epsilon Nd$  data are from Pierson-Wickman et al. (2001) and this study only. Lines are three-point moving averages. Data points shown as circles at *ca.* 16 ka in all graphs are identified as outliers due to non-negligible hemipelagic influence.

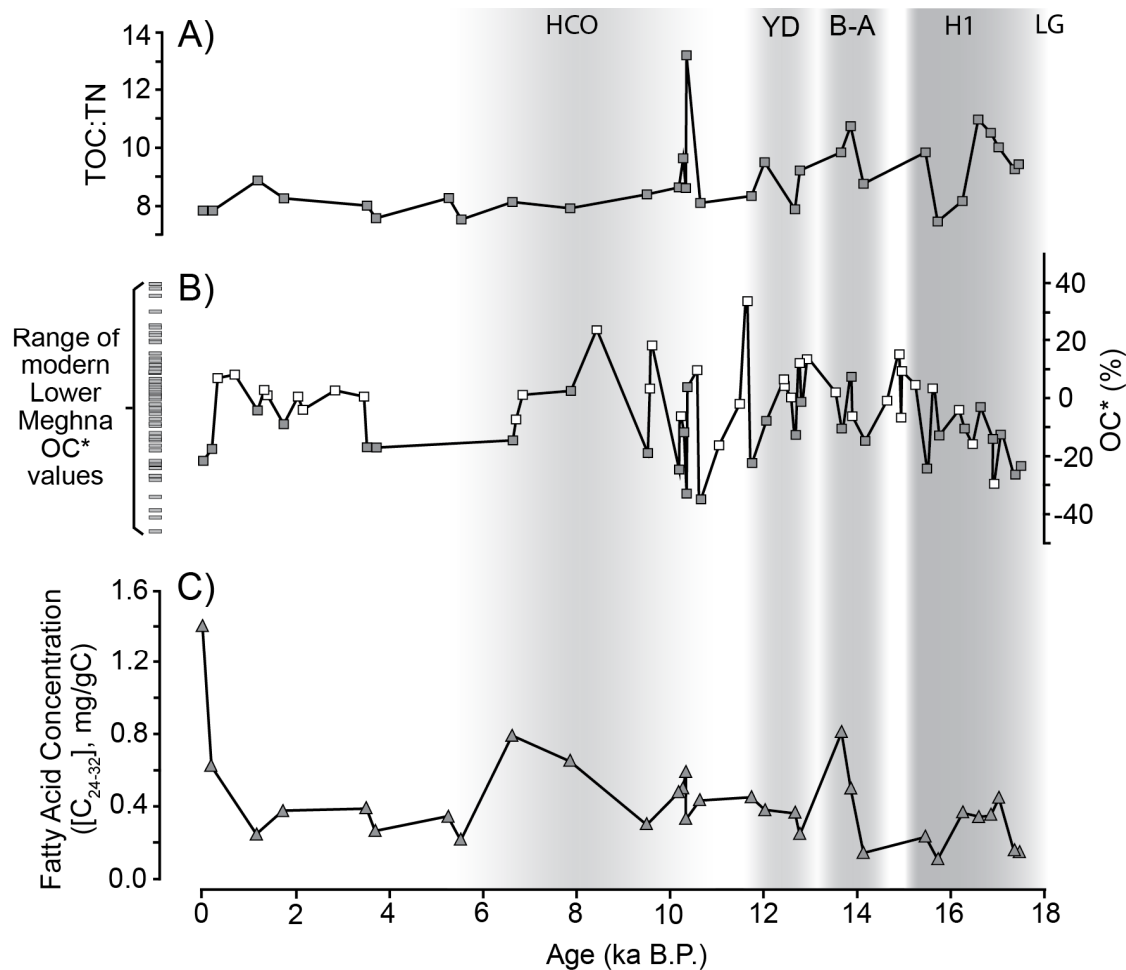


**Figure 5.** G-B river and BoB channel levee (cores SO93-117KL, -118KL, and -120KL) temporal records of (a) bulk sediment TOC:TN ratios; (b) OC\*, the bulk sediment TOC, normalized to Al/Si ratios according to TOC sample preparation method (liquid acidification [open symbols; Galy et al., 2008] vs. fumigation [closed symbols; this study]; see supplemental materials for details), with respect to the modern Lower Meghna River and (c) Concentration of C<sub>24-32</sub> FA, given as a proxy for terrestrial OC, as a function of bulk sediment OC content. River data in (b) are from Galy et al. (2008b) and three outliers (OC\* = 58–103% of modern rivers; data included in Supplemental Table 2) are omitted from (b) due to likely inclusion of marine OC (hemipelagic) or terrestrial vegetation debris.

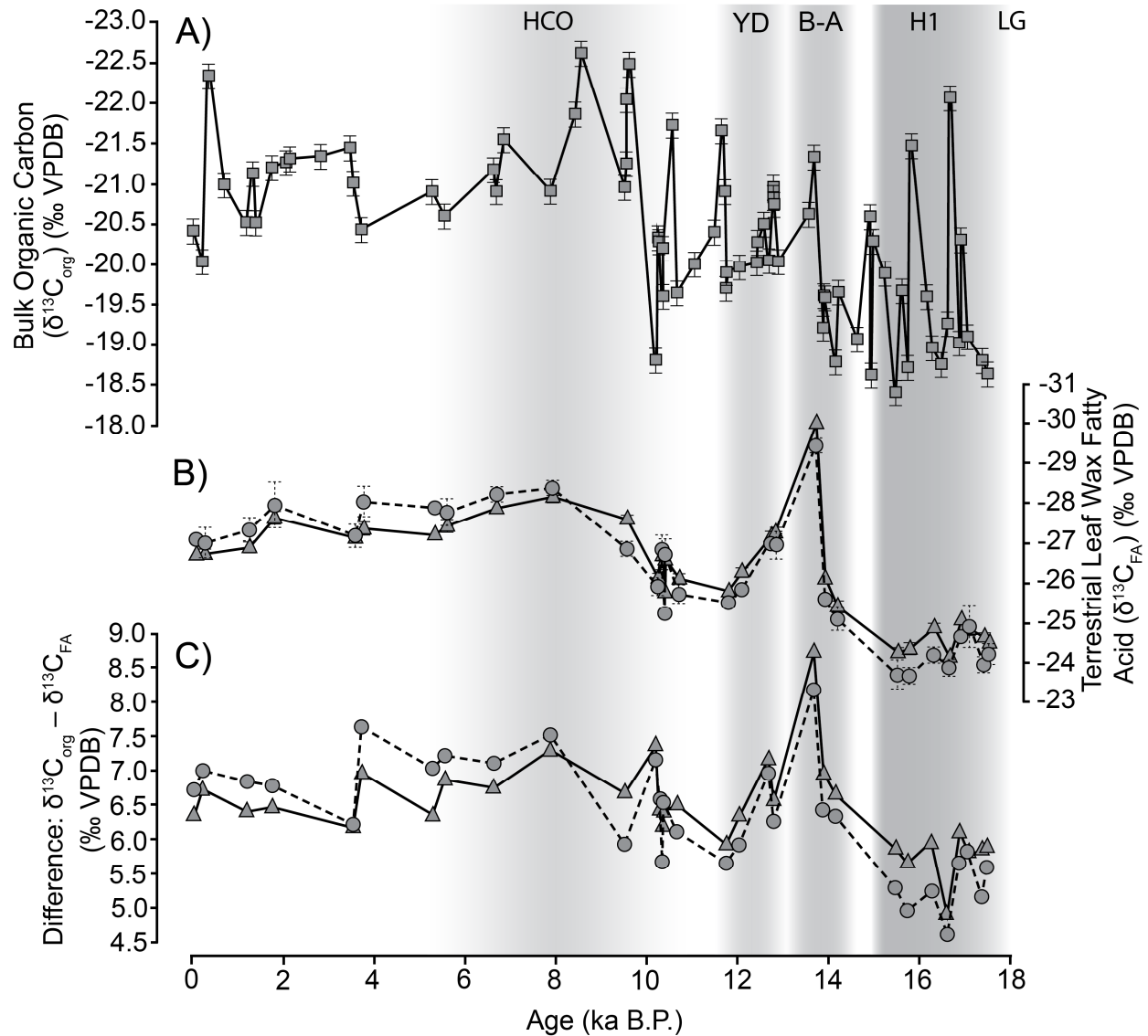


**Figure 6.** Temporal evolution of stable carbon isotopic compositions of sediments and leaf wax fatty acids from BoB channel levee cores SO93-117KL, -118KL, and -120KL (this study only). (a) Bulk sediment  $\delta^{13}C_{org}$  values; (b) Compound-specific  $\delta^{13}C_{FA}$  values for C<sub>24-32</sub> (triangles) and C<sub>28</sub> (circles) FAMES. (c) Difference between compound-specific  $\delta^{13}C_{FA}$  values for C<sub>24-32</sub> (triangles) and C<sub>28</sub> (circles) FAMES and bulk sediment  $\delta^{13}C_{org}$  values. Errors are within data points where error bars not shown.



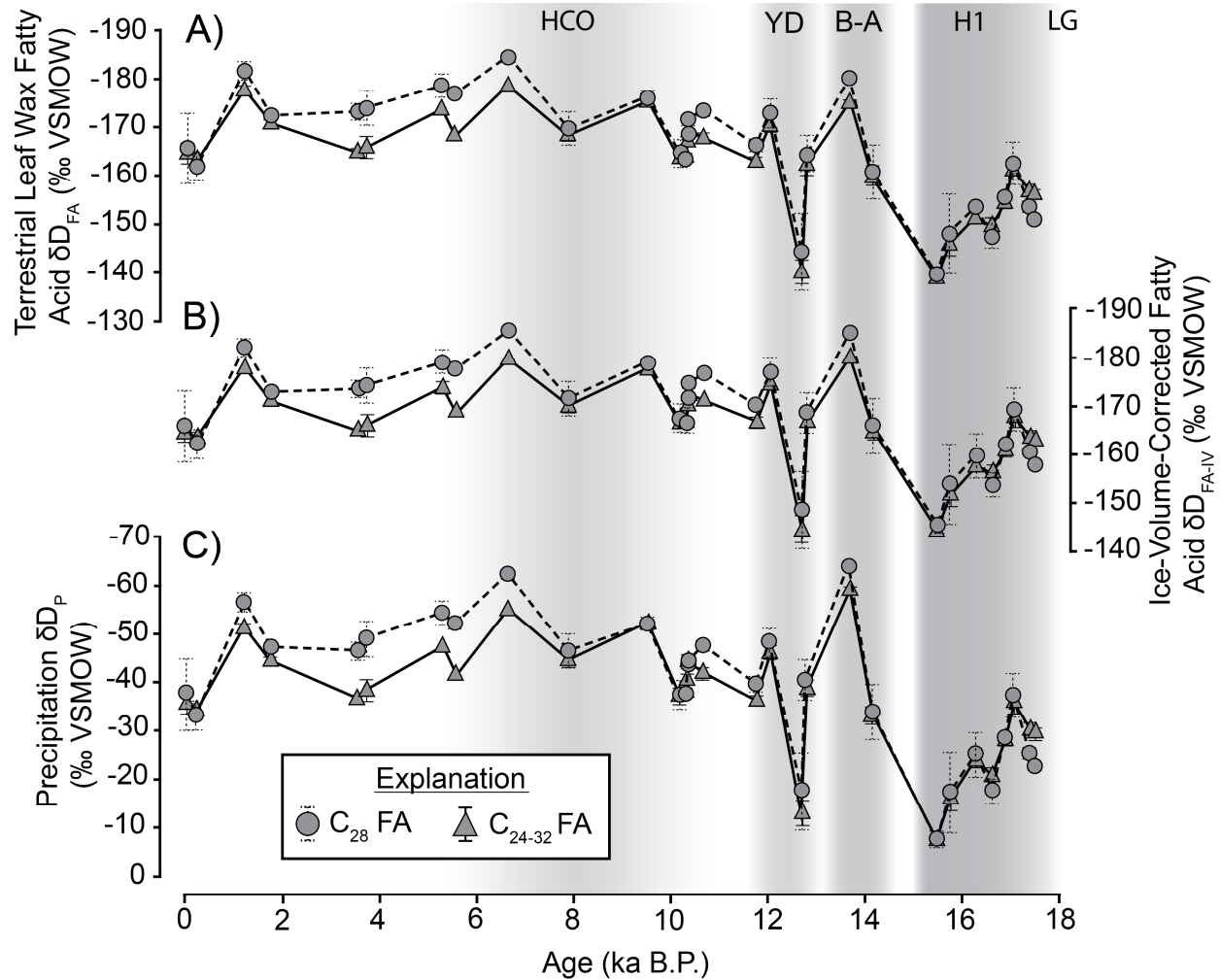


**Figure 7.** Temporal evolution of stable hydrogen isotopic compositions of leaf wax fatty acids and G-B basin precipitation derived from BoB channel levee cores SO93-117KL, -118KL, and -120KL. (a) Methanol-corrected compound-specific  $\delta D_{FA}$  values for  $C_{24-32}$  (triangles) and  $C_{28}$  (circles) leaf wax fatty acids. (b)  $C_{24-32}$  (triangles) and  $C_{28}$  (circles) leaf wax fatty  $\delta D_{FA}$  values corrected for ice-volume effects. (c) Precipitation  $\delta D_P$  values calculated from ice-volume-corrected leaf wax fatty  $\delta D_{FA-IV}$  and basin-integrated vegetation compositions inferred from  $\delta^{13}C_{FA}$  values. Errors are within data points where error bars not shown.

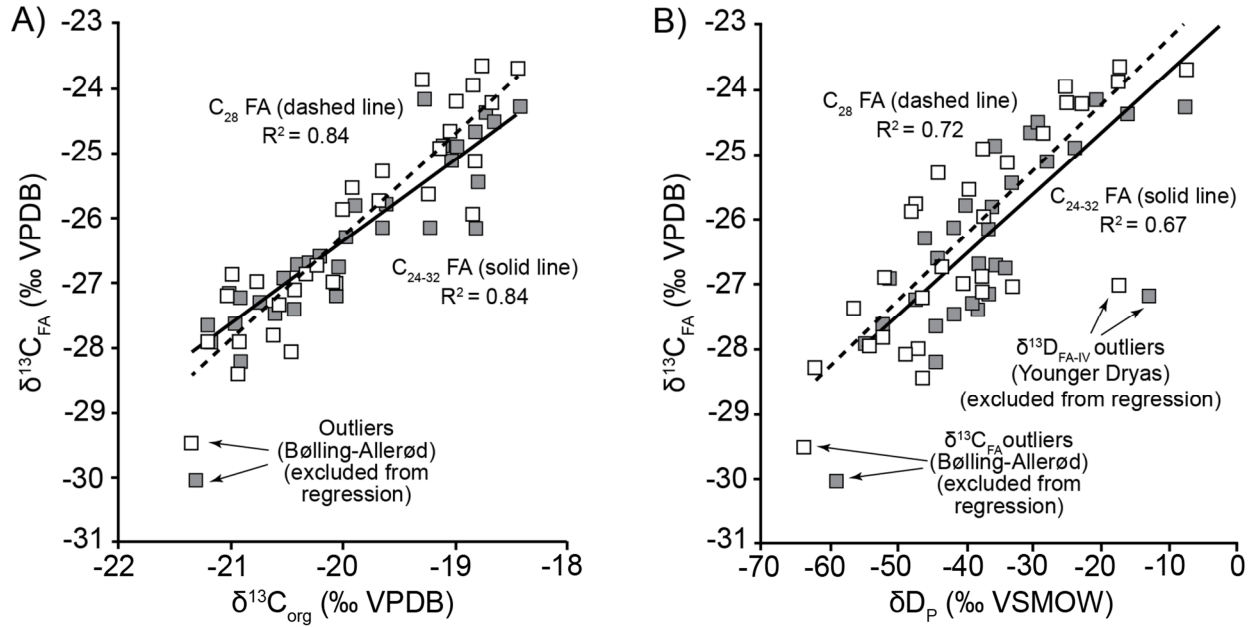


**Figure 8.** Stable isotopic compositions of sediments and FAMES from BoB channel-levee cores SO93-117KL, -118KL, and -120KL. (a) Comparison of bulk  $\delta^{13}\text{C}_{\text{org}}$  values and compound – specific  $\delta^{13}\text{C}_{\text{FA}}$  values for  $\text{C}_{24-32}$  (filled symbols) and  $\text{C}_{28}$  (open symbols) leaf wax fatty acids. (a) Comparison of compound-specific  $\delta^{13}\text{C}_{\text{FA}}$  and  $\delta\text{D}_\text{P}$  values for  $\text{C}_{24-32}$  (filled symbols) and  $\text{C}_{28}$  (open symbols) leaf wax fatty acids.



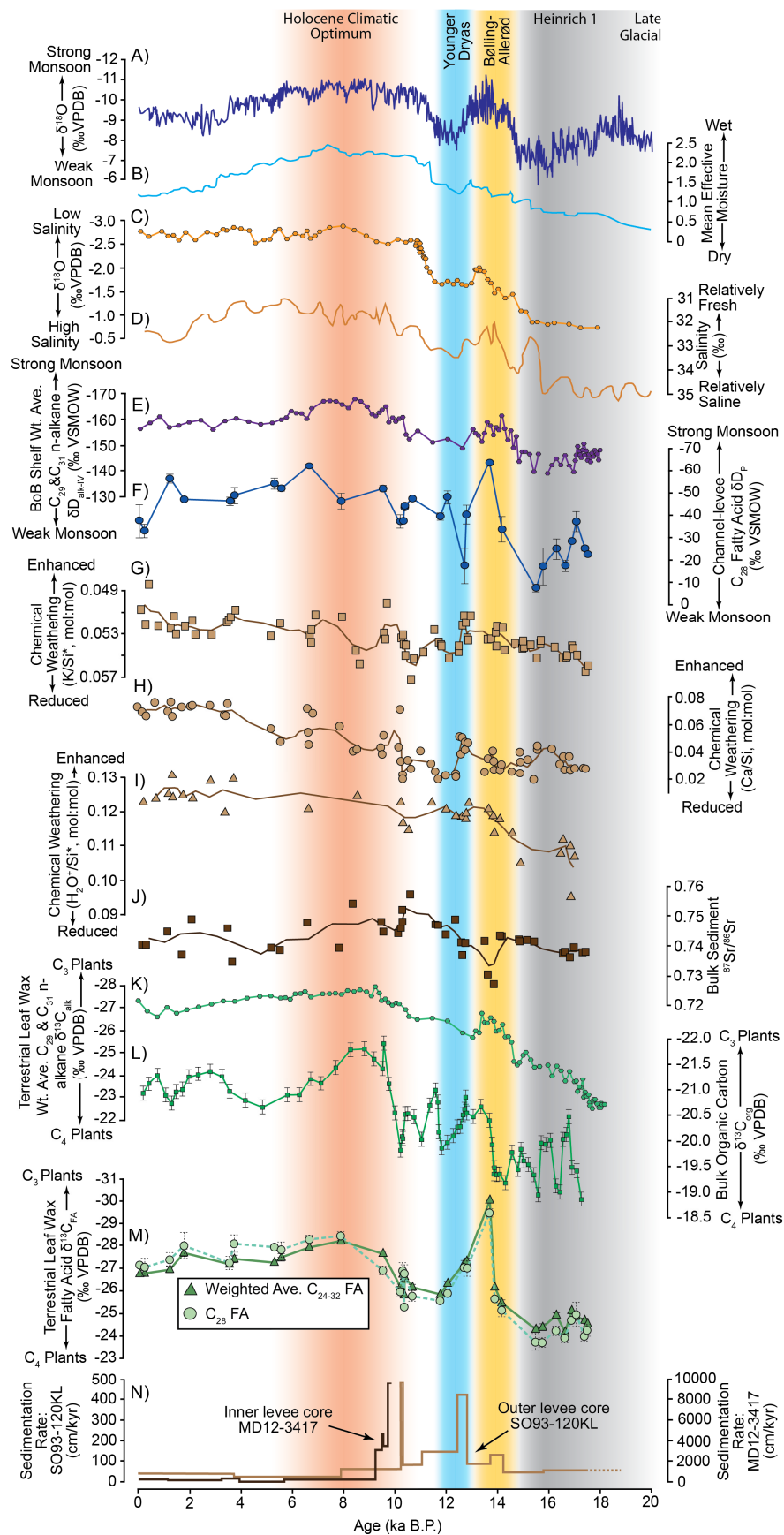


**Figure 9.** Comparison on summer monsoon records and records of response in the G-B basin and BoB following the last glacial maximum. (a) Composite Chinese cave speleothem  $\delta^{18}\text{O}$  record (Cheng et al., 2016); (b) mean effective moisture in central Asia (Herzschuh, 2006); (c) three-point moving average of  $\delta^{18}\text{O}$  of planktonic foraminifers (*G. ruber*) from BoB channel-levee cores (SO93-117KL, -118KL, and -120KL) (data from Galy et al. [2008a] and Weber et al. [1997]); (d) BoB sea-surface salinity, as derived from foraminifera  $\delta^{18}\text{O}$  records (Kudrass et al., 2001); (e) ice-volume-corrected compound-specific hydrogen isotope compositions ( $\delta\text{D}_{\text{ALK-IV}}$ ) of plant wax n-alkanes from Bengal Shelf core SO188-342KL (Fig. 2a), sourced from likely mix of G-B basin and Indo-Burman (I-B) range (Contreras-Rosales et al., 2014); (f) ice-volume- and vegetation-fractionation- corrected fatty acid  $\delta\text{D}_\text{P}$  values from channel-levee cores, sourced solely from G-B basin (this study; see Fig. 7c); (g) data and three-point moving average of terrestrial chemical weathering proxy record ( $\text{K}/\text{Si}^*$ ; see Fig. 4a); (h) data and three-point moving average of terrestrial chemical weathering proxy record ( $\text{Ca}/\text{Si}$ ; see Fig. 4b); (i) data and three-point moving average of sediment hydration, a proxy for terrestrial chemical weathering, from the BoB channel-levee system (Lupker et al., 2013); (j) data and three-point moving average of sediment source proxy record from the BoB channel-levee system ( $^{87}\text{Sr}/^{86}\text{Sr}$ ; see Fig. 4c); (k) compound-specific  $\delta^{13}\text{C}_{\text{ALK}}$  compositions (vegetation type sources) of plant wax n-alkanes from Bengal Shelf core SO188-342KL (Contreras-Rosales et al., 2014); (l) 3-pt. moving average of bulk  $\delta^{13}\text{C}_{\text{org}}$  channel-levee cores (data from Galy et al. [2008a], Galy et al. [2014], and this study); (m) compound-specific  $\delta^{13}\text{C}_{\text{FA}}$  compositions of plant wax n-alkanoic (fatty) acids from channel-levee cores (this study; see Fig. 6b); (n) sedimentation rate for outer channel-levee core SO93-120KL (this study) and inner levee core MD12-3416 (Fournier et al., 2016).

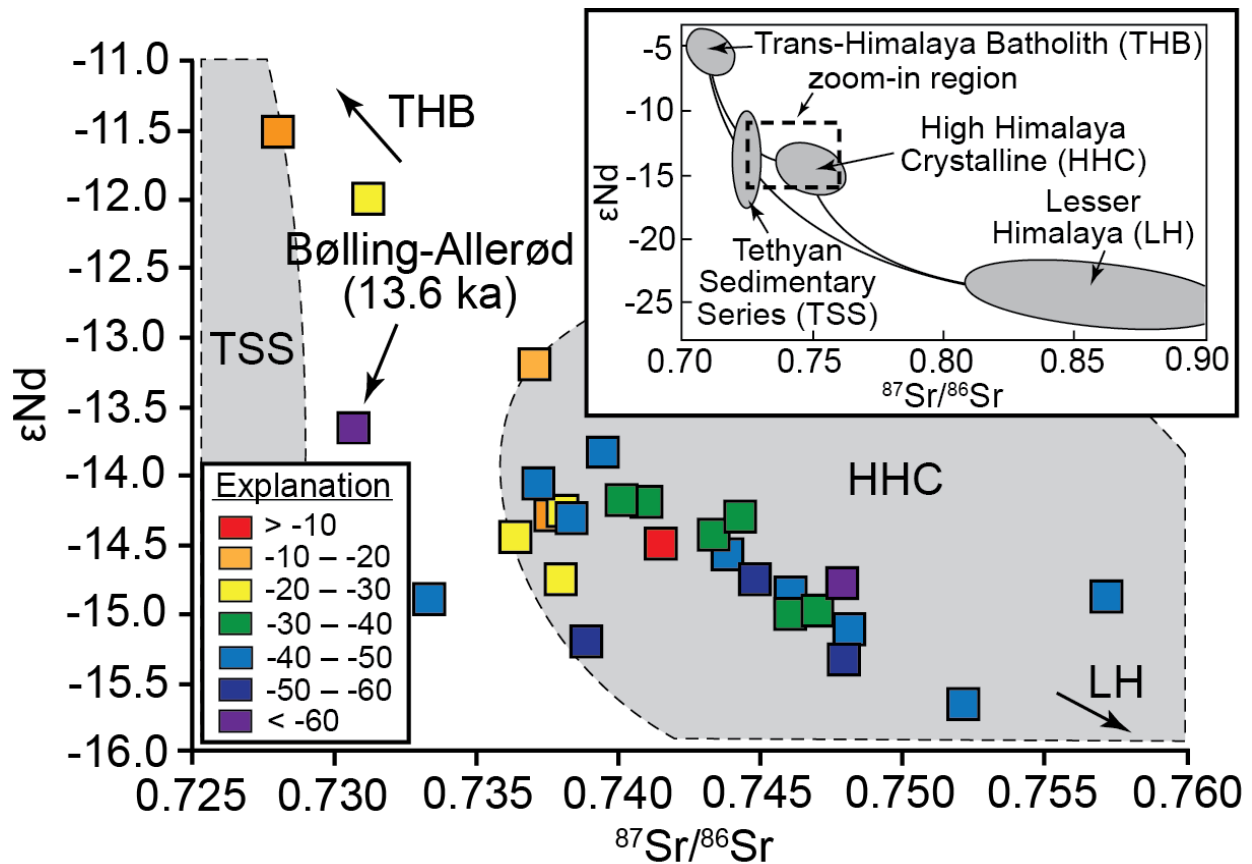


**Figure 10.** Sr–Nd isotope mixing plot of sediments from BoB channel-levee cores SO93-117KL, -118KL, and -120KL (this study only), color-coded by precipitation  $\delta D_p$  values calculated from leaf-wax fatty acid  $\delta D_{\text{FA-IV}}$  values derived from those same samples. Note that  $\epsilon_{\text{Nd}}$  values of two most enriched samples (upper left) likely have some contribution from hemipelagic sediments (see Supplemental Fig. 6). Inset: Sr–Nd isotope mixing plot showing the major lithologic units of the Himalayan range (inset modified from Galy et al. [2010]; TSS data field are from Bouquillon et al. [1990], France-Lanord, et al. [1993], Galy and France-Lanord [1999], and Robinson et al. [2001]).